Int j simul model 21 (2022) 3, 453-464
Original scientific paper

ANALYSIS OF PUMPING STATION INLET CHARACTERISTICS BASED ON VORTICITY

Xi, W.[*]; Lu, W. G.[*,#]; Wang, C.[*,**] & Liu, J. F.[*]
[*] College of Hydraulic Science and Engineering, Yangzhou University, Yangzhou, 225009, China
[**] International Shipping Research Institute, Gongqing Institute of Science and Technology, Jiujiang, 332020, China
E-Mail: wglu@yzu.edu.cn ([#] Corresponding author)

Abstract
This study aims to solve this problem and understand the formation mechanism of the vortex attached to the side pump sump. Thus, numerical simulations were conducted using the calculation software, and the flow characteristics of the side pump sump were studied based on the vorticity field. The flow field data of the physical model of the pumping station forebay and pump sump were obtained by particle image velocimetry. The distribution of vorticity in the different flow layers and vertical axes at the study location was obtained using Tecplot postprocessing software and corroborated with the results of the numerical simulations. This basis was used to analyse the mechanism of the formation of the adherent vortex. Results show that the inflow distribution is uneven and the water flow resistance and vortex strength are imbalanced due to the asymmetry of the vorticity of the inflow of the side pump sump. This causes the attachment of the vortex to the wall, which causes the generation of the suction vortex, vibration of the unit, and instability of the overcurrent, endangering the safety of the project.
(Received in April 2022, accepted in July 2022. This paper was with the authors 1 month for 1 revision.)

Key Words: Pump Station Engineering, Side-Pump Sump, Vorticity, Adherent Vortex

1. INTRODUCTION

Pumping stations are water-lifting structures used for energy conversion and transmission. These structures are used in agricultural irrigation, disaster mitigation and prevention, industrial enterprises, and urban drainage. A proper hydraulic design provides good water intake conditions for the pumps and improves their operating efficiency. The structural form of the forebay and pump sump determines the inflow conditions of the pumping station project. A mechanistic study of the complex flow regime in the forebay and pump sump is helpful for improving the safety, efficiency, and design of the pumping station operation. In the actual operation of multiunit pumping stations, the side unit is prone to uneven inlet flow, which causes lateral flow and vortex phenomena. These conditions result in a low flow rate in the side pump sump, which causes unit vibration and affects the pump efficiency and pumping station safety. Numerical simulation methods for turbulence have been widely used in the engineering field with the advent of fluid simulation software.

As an increasing number of large- and medium-sized pumping stations are built, the complex flow patterns in the inlet basin do not meet the requirements for safe pumping station operation in pumping station engineering. Therefore, it is important to analyse the causes of the vortices in the sump of the pumping station. Direct numerical simulation (DNS) [1, 2] is more accurate; however, it can lead to long calculation times owing to the large range of simulations required for pumping station projects. The Reynolds averaging method called Reynolds-averaged Navier–Stokes (RANS) [3, 4] is the dominant calculation method in engineering. It allows for calculations over a large range of flow fields and has small computational volumes; however, it has many limitations and does not allow deeper studies of important structures in engineering. In contrast, the large eddy simulation (LES) method [5] can resolve all large-scale flows with a well-adjusted grid, which makes it easier than RANS to show the variation in eddies. However, little research is available on the use of LES methods in pumping station

engineering [6]. A detailed analysis has been conducted using numerical simulations, but no physical model verification of the results has been performed. In terms of physical model testing, a large physical model using DPIV has been developed. The measurement range of the model is wide, and it is closer to actual engineering. However, this method requires a highly physical model and high cost. Point and surface flow field measurements using LDV and particle image velocimetry (PIV) [7] and bulk flow field measurements using V3V have also been proposed. However, these methods have a small measurement range, and it is difficult to measure the overall flow-field distribution in a project. Physical modelling studies have also mostly focused on the distribution of flow velocities and less on the distribution of vortex fields.

2. STATE OF THE ART

A comparative study of the flow field flow patterns in the side and non-side pump sump has been proposed to analyse the flow pattern in the side pump sump and the vortex formation mechanism. Several scholars have conducted relevant research on the following aspects: In their research on vorticity, Couch and Krueger [8] studied the interaction of vortex rings with tilted boundaries. They found that the asymmetry in the flow increases as the vortex interaction with the boundary evolves, and the dissipation of kinetic energy is more rapid for higher incidence angles. However, the study was conducted on inclined slabs and only performed physical modelling, ignoring extensive numerical simulation calculations. Liu et al. [9] proposed a new vector called Rortex to better describe the vortex field. It can accurately describe the local fluid rotation and display vortical structures. Vela-Martín [10] studied the dynamics of strong vorticity through synchronization experiments, and found that the stretching of the vortex vector by the large-scale strain rate tensor leads to strong vortex synchronization. However, this study focuses on theory and is difficult to apply directly to engineering.

In research on wall turbulence, Hoyas and Jiménez [11, 12] performed many numerical simulations and theoretical demonstrations with Reynolds numbers in the range of 180–2000 to analyse the wall turbulent motion. However, they only applied numerical simulations to study the flow in the horizontal direction and did not verify the physical model test. Abderrahaman-Elena et al. [13] conducted DNS of a turbulent channel with rough walls in a transitional rough state. They found that the background turbulence begins to be modified as the roughness size increases, especially by the increase in energy for short and wide wavelengths, which is consistent with the appearance of a shear-flow instability of the mean flow. This research is detailed, but not validated by engineering models. Güemes et al. [14] evaluated the applicability of super-resolution generative adversarial networks as a methodology for the reconstruction of turbulent flow quantities from coarse-wall measurements. The method is applied for the resolution enhancement of wall fields and the estimation of wall-parallel velocity fields from coarse wall measurements of shear stress and pressure.

In research on complex open-channel flow regimes, Cater and Williams [15] performed turbulence simulations in a long composite open channel (Re = 42000). A secondary flow is identified at the internal corner, which persists and increases the bed stress on the floodplain. Zeng and Li [16] developed a hybrid RANS model combined with an LES model and used it to simulate the flow of an open-channel T-joint. The results showed that the calculation result of this method is accurate and has significant advantages compared with the traditional LES method. In research on complex open-channel flow patterns, few analyses have introduced vorticity, and no studies related to open-channel flow patterns in pumping station engineering have been conducted.

In a study on the flow around a cylinder, Lam and Lin [17] conducted a 3D numerical simulation of laminar flow around cylinders (Re = 100) of different diameters. They found that the control of flow-induced vibration by changing the spanwise wavelength of the cylinder is

related to the change in the Reynolds number. These studies did not investigate vorticity distribution, and the proposed cylindrical models are difficult to apply in pumping station engineering. Several scholars have used numerical simulation methods [18-21] or physical model tests in fluid studies. Many scholars have also used a combination of the two [22, 23] to verify each other, but few have used a combination of physical model tests and theoretical analysis [24-26].

Numerous scholars have studied the flow distribution in the forebay and sump pumping stations. Song and Liu [27] used a 3D velocity field test system V3V to analyse the velocity gradient, eddy current intensity, and eddy kinetic energy in the vortex region during the evolution of the bottom-attached vortex. They also used it to measure the flow field under the baffle tube of a certain type of ship and a vertical axial flow pump under eddy-current conditions. However, the study was conducted close to the trumpet and did not involve a side pump sump.

The abovementioned studies focus on channel flow, wall turbulence, and surrounding flow, and work on the vortex in the pump sump of a pumping station is mostly concentrated on the inspiratory vortex at the bell mouth. Meanwhile, research on the near-wall vortex in the pump sump, particularly on the formation mechanism of the asymmetric adherent vortex in the pump sump of pump stations, is scarce. Existing research cannot explain the formation mechanism of the vortex in the side inlet pool of the pump station, and the vortex in the side inlet pool seriously affects the normal operation of the pump station. Therefore, it is important to analyse this phenomenon. In this study, the vorticity change in the side pump sump was analysed using a numerical simulation method. A physical model was built, the vorticity field data of the pumping station forebay and pump sump were collected using PIV, and the vorticity distribution map was obtained using Tecplot post-processing software. The results and the numerical simulation calculation results were verified. Considering the results of the physical model and numerical simulation, the formation mechanism of vorticity symmetry in the side pump sump and non-side pump sump was analysed. This study provides theoretical help for solving the problem of vortices in the side inlet pool of a pumping station project.

The remainder of this paper is organized as follows. The modelling of the pumping station inflow, the test process of the PIV model, and the verification of the physical model and numerical simulation are described in Section 3. The time independence of the vorticity field in the inlet pool of the pumping station is studied through numerical simulation results, and the uneven distribution of the vorticity in the inlet pool at the side of the pumping station is summarized in Section 4. The entire text is summarized, and relevant conclusions are presented in Section 5.

3. METHODOLOGY

3.1 Numerical simulation

Calculation equation: According to the vortex theory of turbulent flow, large-scale eddies are the main causes of turbulent pulsation and mixing. Large-scale eddies derive their energy from the main flow of the flow field, are highly anisotropic, and vary with flow conditions. Large-scale vortices transfer energy to small-scale eddies through interaction. Small-scale eddies primarily dissipate energy in the flow field, are nearly isotropic, and have many commonalities in different flow situations. The abovementioned theory introduces the numerical solution of the LES. This method uses the unsteady Navier–Stokes (N–S) equation to directly solve large-scale eddies and a sublattice stress model to approximate the effect of small eddies on large eddies. The large eddies are solved directly, the small-scale eddies are solved by the model, and the influence of the small eddies on the large eddies is considered by an approximate model. LES contains different methods for solving the subgrid-scale turbulent viscosity.

After filtering the 3D turbulent N–S equation with the spatial filter function, the governing equation of the large-eddy model is obtained as follows:

$$\frac{\partial \rho}{\partial t}+\frac{\partial \rho u_i}{\partial x_i}=0 \tag{1}$$

The Reynolds equation is:

$$\frac{\partial(\rho u_i)}{\partial t}+\frac{\partial(\rho u_i \rho u_j)}{\partial x_j}=-\frac{\partial p}{\partial x_j}+\frac{\partial}{\partial x_j}(\mu \frac{\partial u_i}{\partial x_j})+S_i \tag{2}$$

where x_i and x_j ($i, j = 1, 2, 3$) are Cartesian coordinates and $\overline{u}_i$ and $\overline{u}_j$ ($i, j = 1, 2, 3$) are the velocity components after filtering. $\overline{p}$ is the pressure after filtering. g_i represents the mass force component, and ν represents the molecular viscosity coefficient. τ_{ij} is the sublattice Reynolds stress induced by nonlinear convection in filtering, and $\overline{\tau_{ij}}=\overline{u_i u_j}-\overline{u_i}\,\overline{u_j}$. Therefore, small-scale variables affect large-scale variables, which appear in the equation of motion as a stress term similar to Reynolds stress, called sub-lattice Reynolds stress; it must be simulated by establishing a model. The LES turbulence simulation method assumes that the turbulent motion can be divided into large- and small-scale eddies. The separation of the two inconsiderably affects the evolution of the large eddy current, and the small eddy current is less affected by the flow geometry and boundary conditions. The Smagorinsky model is the most commonly used sub-grid Reynolds stress model based on the eddy viscosity assumption. The LES directly solves a large-scale field using a set of filter control equations. The subgrid scale is isotropic and is primarily used to express dissipation. Thus, its influence on the grid scale can be simulated easily. For this model, a relationship is assumed to exist between the subcrystalline Grenaud stress and the strain rate tensor, as follows:

$$\tau_{\mathrm{ij}}=-2\nu_t \overline{S_{ij}}+\frac{1}{3}\tau_{kk}\delta_{ij},(k=1,2,3) \tag{3}$$

ν_t is the turbulent eddy viscosity coefficient, and $\mathrm{v_t}=(\mathrm{C_s}\Delta)^2\left|\overline{\mathrm{S}}\right|$. x_i is the Smagorinsky coefficient, which has a value between 0.1 and 0.27. $\left|\overline{\mathrm{S}}\right|$ is the value of both $\overline{\mathrm{S_{ij}}}$ and $\left|\overline{\mathrm{S}}\right|=\left(2\overline{\mathrm{S_{ij}}}\,\overline{\mathrm{S_{ij}}}\right)^{\frac{1}{2}}$. Δ denotes the length of the filter grid. $\overline{\mathrm{S_{ij}}}$ is the filtering strain tensor, and $\overline{S_{ij}}=\frac{1}{2}\left(\frac{\partial \overline{u_i}}{\partial x_j}+\frac{\partial \overline{u_j}}{\partial x_i}\right)$. The δ_{ij} is a Kronecker triangular tensor. When $i = j$, $\delta_{ij} = 1$; when $i \neq j$, $\delta_{ij} = 0$. The above-mentioned equations constitute a closed equation for solving the distribution law of the flow field in the side pump sump of the pumping station, and the vorticity field equation can also be constructed. Then, the corresponding boundary conditions are applied according to the actual working conditions to form a definite solution of the equation set.

Boundary conditions and meshing: The upstream inlet section is set as the inlet boundary of the computational domain, and moderate turbulence intensity is specified as $T_u = 5\,\%$. The inlets of the three units of the pumping station are set as the outlet boundaries of the entire computational domain. Each outlet adopts a static pressure boundary condition, and the pressure value is set to 1 atm. The water level does not change significantly, considering the shear stress of the air on the water surface. Except for the inlet, outlet, and free water surface, the rest are solid walls. The number of calculation steps is 2000 steps, and the convergence accuracy is 10^{-7}.

The model is meshed using the WORKBENCH in ANSYS. Unstructured meshing is used for the entire computational domain owing to its complex structure. Local refinement of the grid is performed in the range of the side entry pool, and the hydraulic loss is considered as a suitable parameter to measure the number of grids. When the number of grids reaches

2,677,733, the hydraulic loss remains constant. The difference also does not exceed 2 %, which meets the calculation requirements.

3.2 Physical model method

A test device that can test the flow field of the inlet pool of the pumping station project, which is combined with the three-unit pumping station of an actual project, is designed according to the research needs. The test device is shown in Fig. 1. A circulating water supply is adopted to facilitate the test control. The device consists of a circulating water tank, circulating water pump, inlet chest, steady water board, physical model test section, water-level regulator, and liquid injection tube. The test section consists of the inlet channel, front pool, inlet pool, and flow channel placed horizontally on the support. The length of the test section is 500 mm, width of the inlet pool is 40 mm, thickness of the middle pier is 6 mm, height of the middle pier is 160 mm, and height of the middle pier is 90 mm. The slope section of the pool is 10 mm long, the horizontal section is 30 mm long, and the inlet pool section is 90 mm long. The model is made of a transparent acrylic sheet to facilitate data collection of the flow field of the forebay and side pump sump by PIV.

In the test, the flow-field characteristic data are collected using PIV. This technology can obtain the entire information of the liquid flow in the field of view, and the real-time data required for the analysis are extracted using the relevant software. This method is suitable for collecting liquid flow fields without interference. The PIV test system consisted of a laser transmitter, CCD camera, and synchronizer. In this experiment, the laser operating frequency is 50 HZ, the acquisition speed is 260 frames/s, the interval between two frames is 100 μs, and 600 PIV particle images are captured by the CCD camera each time. Microver software is used for analysis, and the data are further processed using Tecplot software to obtain the vorticity cloud maps of different flow layers and vertical axes of the side pump sump. The plane composed of the abscissa X and ordinate Y in the figure corresponds to the size of the shooting window of the CCD camera. The test is conducted under the condition of constant flow, at a test temperature of 20°C.

During the test, the circulating water pump is turned on to form a stable water flow cycle. The flow rate is adjusted through the valve on the water supply pipe, the water level in the test section is set, and the water level is kept stable. After the water passes through the test model section, it flows into the circulating water tank below. The water flow is circulated in the test device. After the water flow in the test section is stable, the flow field of the forebay and side pump sump corresponding to the research position is collected by the PIV system.

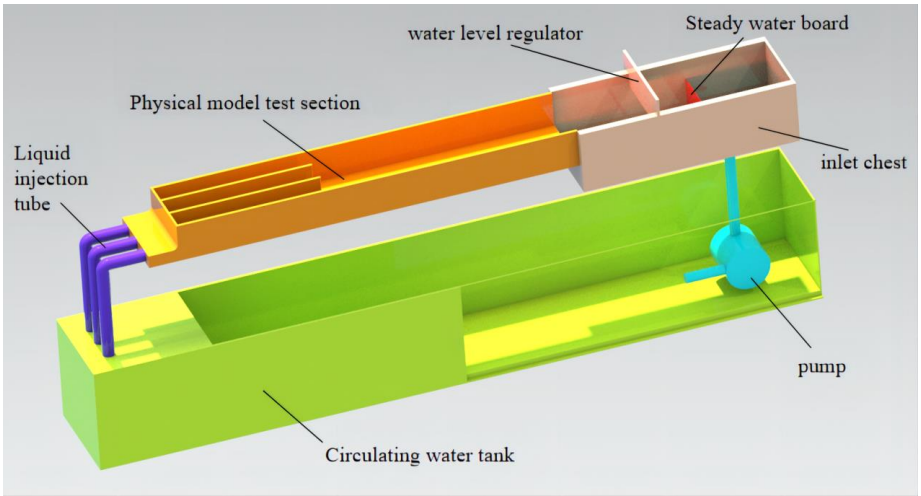

Figure 1: Diagram of the PIV test device.

3.3 Model validation

The PIV technology is used to measure the built physical model for further analysis of the numerical simulation results. The horizontal flow layer and vertical axial flow field in the side and non-side pump sumps are also studied. The numerical simulation results need to be compared with the physical experimental data to verify the reliability of the established mathematical model. The mathematical models of the Froude number, Reynolds number, and flow ratio are consistent with those of the physical experiments. The coordinate system is dimensionless based on the width of the inlet pool, and the velocity is dimensionless based on the average flow velocity at the downstream outlet. A comparison of the flow velocity is shown in Fig. 2 (· is the physical experimental value; – is the numerical simulation value).

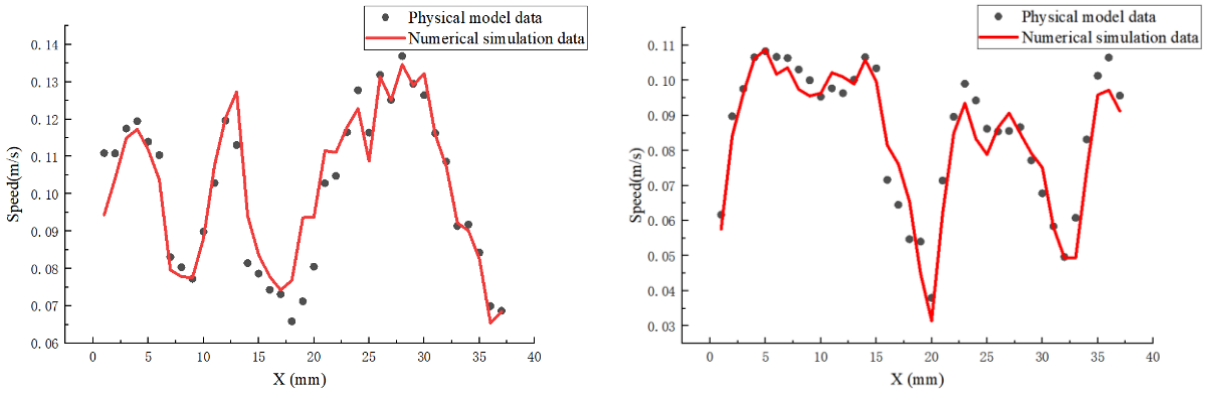

Figure 2: Comparison chart of flow velocity.

4. RESULT ANALYSIS AND DISCUSSION

4.1 2D flow field analysis

Test flow layer selection: In the experiment, horizontal sections of different flow layers are set up in the test section at the junction of the fore and inlet tanks. Five flow layer sections are set at the junction of the forebay and the pump sump. The flow layer 2 m below the water surface line is set as section a, the flow layer 1 cm near the bottom is section e, and the flow layer 0.6 times the water depth is section c. Observation sections b and d are set between sections a and c and between sections c and e to make the flow field data collected along the water depth direction more abundant. It can more comprehensively show the flow fields of different flow layers in the side and non-side pump sumps. The specific cross-sectional positions are shown in Fig. 3.

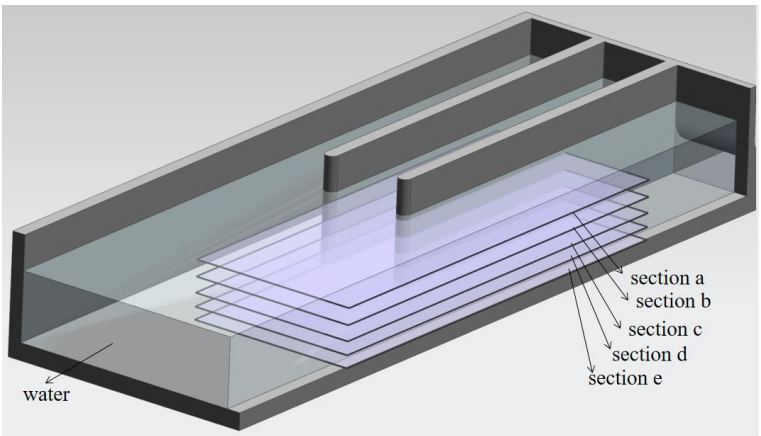

Figure 3: Diagram of section location.

Analysis of vorticity field at different times: The rotation of the fluid micelle motion is expressed in terms of vorticity. Vorticity is a vector that is a function of space coordinates and time, and its spatial distribution determines the vorticity field. A section located near the water surface is selected as the research object, and the vorticity field is extracted every 120 steps (the time step is 0.001 s) to study the change in the vorticity field at different times. Fig. 4 shows the flow fields at different flow times. The vorticity distribution maps are extracted four times in sequence and named as Times 1, 2, 3, and 4. The figure shows that at Time 1, the vorticity distribution on both sides of the pier is relatively dense, the absolute value of the vorticity on the side of the pier close to the side pump sump is larger, the angular velocity of the fluid micelle movement is larger, and the water flow rotates, as is evident here. The vorticity fluctuation in the non-side pump sump is small, and the vorticity in the centre of the flow channel is slightly larger. Meanwhile, the vorticity fluctuation in the side pump sump and the vorticity accumulation near the sidewall and back wall of the edge entry pool are evident. At Time 2, the overall distribution of the vorticity is similar to that at Time 1. The vorticity distribution in the side pump sump is slightly changed, and the larger vorticity distribution is slightly shifted; however, it is still distributed near the side and back walls of the side pump sump. At Times 3 and 4, the overall vorticity is slightly reduced compared to that at Times 1 and 2, but the overall distribution remains the same. Other sections are also analysed, and all show the same trends.

The above-mentioned analysis indicates that the overall distribution and changing law of the vorticity field at different times are consistent, the fluctuation is small, and the periodic change is not obvious. The vorticity field in this study is less affected by time and can be regarded as a steady-state vorticity field for research.

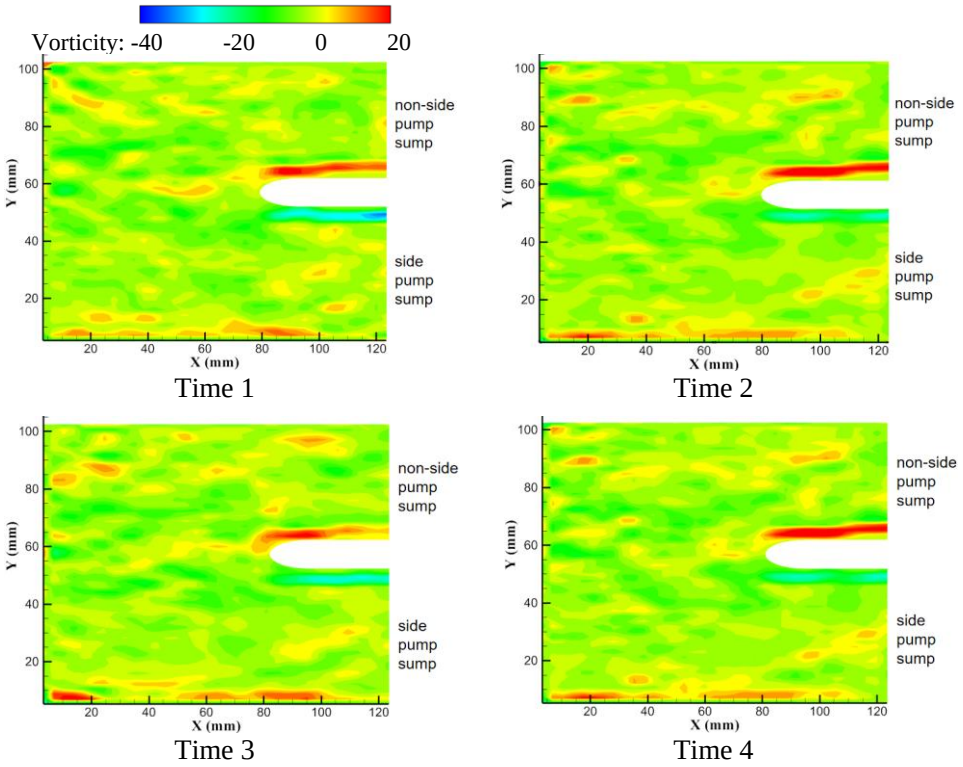

Figure 4: Vorticity field of horizontal section at different times.

Analysis of vorticity field in different layers: The vortex is usually measured by vorticity to determine its strength and direction. In the fluid, vortices of different sizes are generated as long as a "vortex source" is available. Fig. 5 shows the contour distribution diagram of the flow-field vorticity in the different horizontal sections. As shown in section a, the vortices on both sides of the pier are concentrated, long strips of adherent vortices with opposite directions are

formed in the non-side and side pump sump, and long strips are attached to the sidewalls. A vortex zone appears, and the inner centres of the non-side and side pump sumps have large vorticities. The vorticity distributions of sections b and a are similar. Section c was at two-thirds of the water depth. The water flow in the section is turbulent, the vorticity accumulation is evident, and the vorticity of the reverse vortex bands on both sides of the pier increases. The fluid swirl also intensifies. In section d, the length of the inverse vortex band on both sides of the pier decreased along the flow direction and developed laterally. It becomes larger and accumulates on the side and rear walls. The vorticity distribution of section e is close to that of section d, but the overall vorticity is small.

The above-mentioned analysis reveals that the vortex band on the side pump sump is maintained near the wall on the upper three surfaces, and the vorticity gradually decreases on the lower two surfaces. Meanwhile, the vorticity distribution on the sidewall side of the side pump sump is significantly larger than that on the pier side. The energy attenuation of the fluid microclusters on both sides of the pier is faster than that between the fluid microclusters on the wing wall side of the side pump sump, which are only subjected to the frictional action of the leading edge of the pier and diaphragm wall. The piers directly affect the attenuation of the energy in the side and non-side pump sumps, which results in uneven energy changes in the side and non-side pump sumps of the same width. This phenomenon directly affects the efficiency and safety of pumping-station projects.

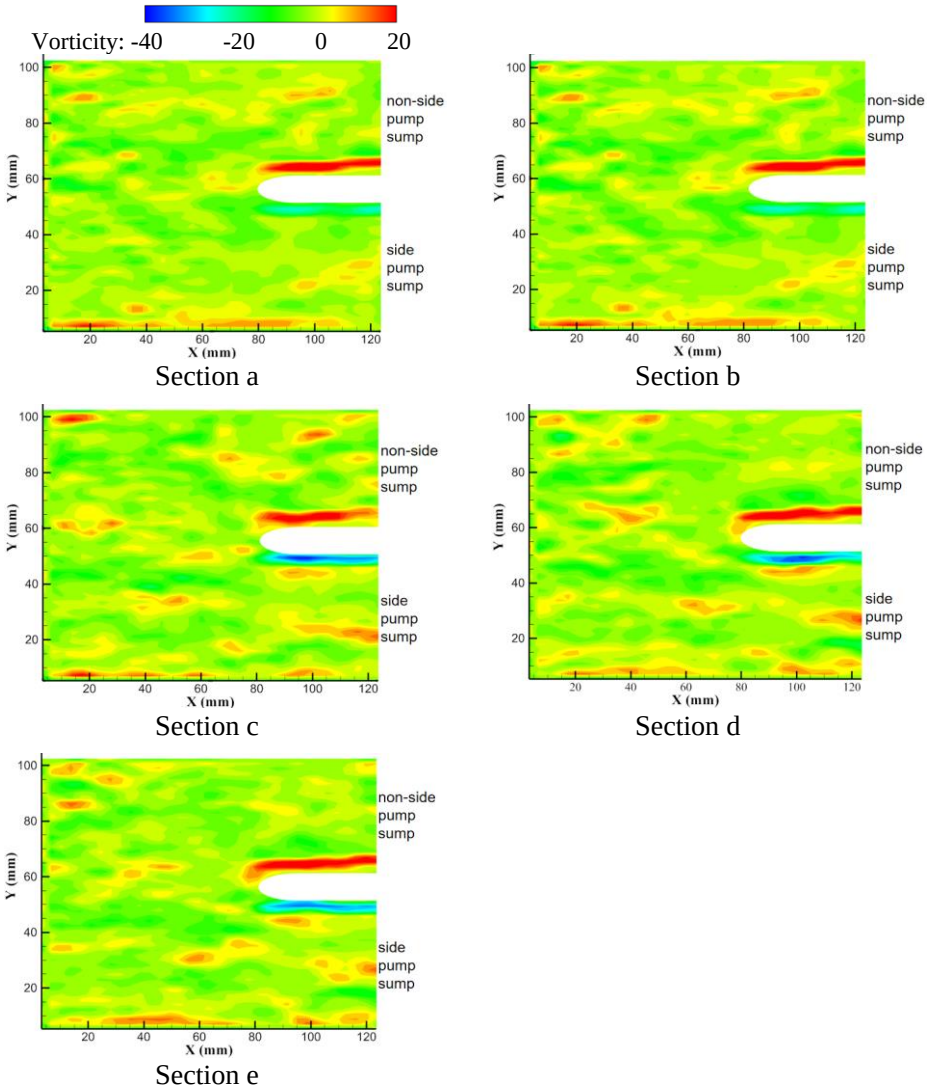

Figure 5: Vorticity field of horizon cross sections of different flow layers.

4.2 Analysis of the characteristics of section

The vorticity field in the sump pump is analysed using software, and the vorticity field of the horizontal flow layer with different water depths is selected. The cross-sectional distributions are shown in Fig. 6. These sections are section 1 of the pump sump section, section 2 immediately before entering the pump sump, section 3 on the rear side of the pier, and section ·4 near the rear wall. The vorticity of the section perpendicular to the flow direction of the water flow is extracted for analysis, and the change in the liquid micelles in the flow direction is explored.

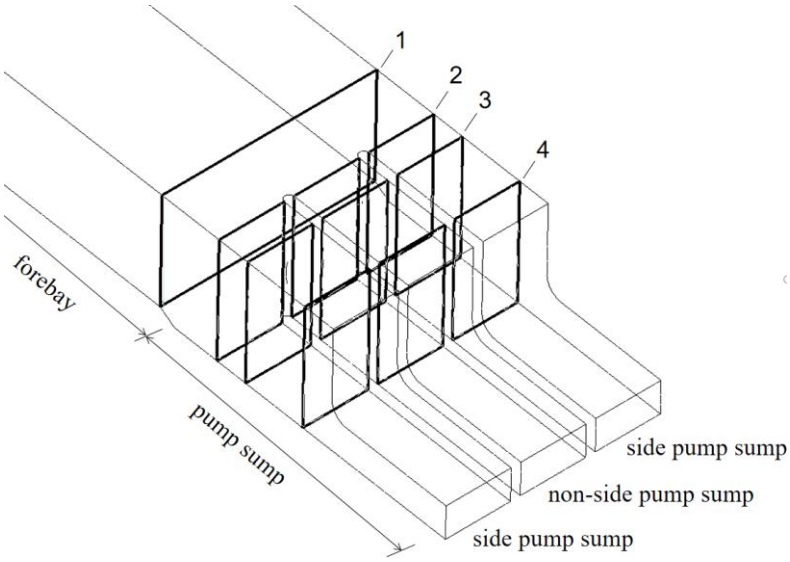

Figure 6: Diagram of section location.

Fig. 7 shows the flow velocity distribution diagram of the vertical section at different positions. Notably, the zero point of the abscissa axis is the position of the pier, the position of x = 44-52 mm is the pier, and the ordinate is the vorticity. The figure shows that the vorticity distribution is more stable in the vertical direction at different water depths in front of the bulkhead in Section 1. The vorticity is smaller in the middle three sections, whereas the vorticity near the water surface is slightly larger than that in the middle section. The vorticity near the bottom is larger, and the vorticity distribution gradually becomes larger in the position near the sidewall. This is because section e is affected by the sidewall and bottom surface, which facilitates the formation of turbulent flow with higher vorticity. Meanwhile, section a is affected by the free liquid surface, which causes the fluid to swirl. In Section 2, the vorticity fluctuates significantly in the vertical direction, and the vorticity gathers on both sides of the septum. The vorticity is smaller in the middle of the side into the pool, reaches a maximum near the sidewall, and maintains a larger value in the vertical direction. However, the vorticity is smaller at the bottom. Therefore, the section immediately before entering the septum is sharply contracted and has evident water flow turbulence and fluid rotation because of the boundary constraint and viscous effects between the liquid microclusters. In Section 3, the vorticity distribution is gradually uniform and less fluctuating, and the vorticity on both sides of the pier is still maintained at a higher value. As the water depth increases, the vorticity on both sides of the pier gradually increases. This is because the water completely enters the sump pump and gradually becomes smooth. However, on both sides of the pier, the fluid easily experiences swirling owing to the wall effect. In Section 4, the eddies are higher on both sides of the face pier and gradually increase with the increase in water depth in the middle of the non-side pump sump and at the sidewalls of the side pump sump. In the bottom section, the vorticity is larger and fluctuates constantly. This is because the longitudinal tumbling of the fluid begins to

increase owing to the action of the back wall and sidewall of the pump sump. The overall analysis concludes that the vorticity distribution in the side pump sump is very uneven, the vorticity on both sides of the side pump sump is larger, and both sides near the wall surface have positive and negative vorticities. Therefore, the flow pattern is highly turbulent with vortices in opposite directions on both sides of the side pump sump. The non-side pump sump, except for the pier near the wall surface of the larger vorticity, has a more uniform vorticity distribution with vorticity values in a small range of fluctuations and a relatively smooth overall vorticity distribution. This finding indicates a more symmetrical distribution of water in the non-side pump sump along the flow direction, with no obvious vortices.

Analysis of the cross-sectional vorticity distribution shows that the microclusters of water entering the side pump sump are more stable. The rotation of the microclusters on the side near the sidewall is stronger because of the action of the sidewall, and the rotation of the microclusters at the pier by the leading edge of the pier is stronger when passing through the pier. Swirling weakens on the backside of the pier but spreads throughout the water. After entering the side inlet basin, the microclusters begin to spin violently owing to the action of the back wall surface and sidewall. This phenomenon created a vertical spiral flow on the backside of the side inlet basin, which generates vortices.

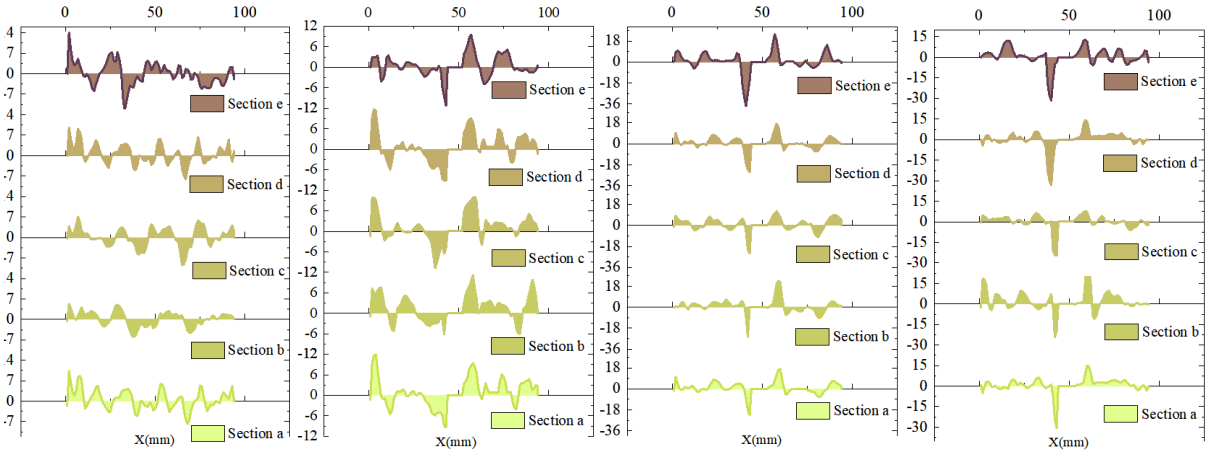

Figure 7: Diagram of numerical simulation cross-sectional vorticity field.

5. CONCLUSION

This study aims to address the problem of a pumping station project in which the side pump sump is prone to produce a wall vortex, which affects the normal safe operation of the pumping station. Thus, numerical simulation methods were used to calculate the sump of a three-unit pump-pumping station. A physical model of the pump sump of a three-unit pumping station with data collection for PIV was established, and a vortex diagram obtained from the collected data was used to verify the numerical simulation results. The following conclusions are drawn.

(1) The vortex field is asymmetrical at both walls in the side pump sump, and the vortex in the side pump sump exhibits an increasing trend at the sidewalls. Therefore, the microcluster rotation of the flow increases in this region, and the vortex symmetry imbalance gradually increases.

(2) The vortex field asymmetry at the two walls of the side pump sump is different from that at the two walls of the non-side pump sump. The imbalance in the side pump sump was greater than that in the non-side pump sump.

(3) The asymmetry of the vortex field triggers changes in frictional resistance to produce inlet vortices.

The analysis was mainly conducted using numerical simulation calculations and validated with physical model tests before vortex asymmetry was introduced for a multi-program study. The research shows that the main cause of the high incidence of eddy currents in the side pump sump of the pump station is the asymmetric distribution of the incoming and outgoing eddy current fields caused by its structural arrangement. This study has important guiding significance for the adjustment of the flow state of a sump pump at a pump station.

ACKNOWLEDGEMENT

The study was supported by the National Natural Science Foundation of China (No. 52079120), Key Laboratory of Modern Agricultural Equipment and Technology (Jiangsu University), Ministry of Education (No. NZ201604), Jiangsu Graduate Research and Innovation Program (KYCX20_2980) and the Priority Academic Program Development of Jiangsu Higher Education Institutions (PAPD).

REFERENCES

[1] Zhu, H.; Liu, W.; Zhou, T. (2020). Direct numerical simulation of the wake adjustment and hydrodynamic characteristics of a circular cylinder symmetrically attached with fin-shaped strips, *Ocean Engineering*, Vol. 195, Paper 106756, 20 pages, doi:10.1016/j.oceaneng.2019.106756

[2] Fabregat, A.; Gisbert, F.; Vernet, A.; Dutta, S.; Mittal, K.; Pallarès, J. (2021). Direct numerical simulation of the turbulent flow generated during a violent expiratory event, *Physics of Fluids*, Vol. 33, No. 3, Paper 035122, 13 pages, doi:10.1063/5.0042086

[3] Larsen, B. E.; Fuhrman, D. R. (2018). On the over-production of turbulence beneath surface waves in Reynolds-averaged Navier-Stokes models, *Journal of Fluid Mechanics*, Vol. 853, 419-460, doi:10.1017/jfm.2018.577

[4] Heinz, S.; Mokhtarpoor, R.; Stoellinger, M. (2020). Theory-based Reynolds-averaged Navie-Stokes equations with large eddy simulation capability for separated turbulent flow simulations, *Physics of Fluids*, Vol. 32, No. 6, Paper 065102, 21 pages, doi:10.1063/5.0006660

[5] Yang, X. I.; Griffin, K. P. (2021). Grid-point and time-step requirements for direct numerical simulation and large-eddy simulation, *Physics of Fluids*, Vol. 33, No. 1, Paper 015108, 9 pages, doi:10.1063/5.0036515

[6] Wang, Y.; Zhang, F.; Yuan, S.; Chen, K.; Wei, X.; Appiah, D. (2020). Effect of URANS and hybrid RANS-large eddy simulation turbulence models on unsteady turbulent flows inside a side channel pump, *Journal of Fluids Engineering*, Vol. 142, No. 6, Paper 061503, 18 pages, doi:10.1115/1.4045995

[7] Cozzi, F.; Coghe, A.; Sharma, R. (2018). Analysis of local entrainment rate in the initial region of isothermal free swirling jets by stereo PIV, *Experimental Thermal and Fluid Science*, Vol. 94, 281-294, doi:10.1016/j.expthermflusci.2018.01.013

[8] Couch, L. D.; Krueger, P. S. (2011). Experimental investigation of vortex rings impinging on inclined surfaces, *Experiments in Fluids*, Vol. 51, No. 4, 1123-1138, doi:10.1007/s00348-011-1135-x

[9] Liu, C.; Gao, Y.; Tian, S.; Dong, X. (2018). Rortex – a new vortex vector definition and vorticity tensor and vector decompositions, *Physics of Fluids*, Vol. 30, No. 3, Paper 035103, 13 pages, doi:10.1063/1.5023001

[10] Vela-Martín, A. (2021). The synchronisation of intense vorticity in isotropic turbulence, *Journal of Fluid Mechanics*, Vol. 913, Paper R8, 11 pages, doi:10.1017/jfm.2021.153

[11] Hoyas, S.; Jiménez, J. (2008). Reynolds number effects on the Reynolds-stress budgets in turbulent channels, *Physics of Fluids*, Vol. 20, No. 10, Paper 101511, 9 pages, doi:10.1063/1.3005862

[12] Hoyas, S.; Jiménez, J. (2006). Scaling of the velocity fluctuations in turbulent channels up to $Re_\tau = 2003$, *Physics of Fluids*, Vol. 18, No. 1, Paper 011702, 4 pages, doi:10.1063/1.2162185

[13] Abderrahaman-Elena, N.; Fairhall, C. T.; García-Mayoral, R. (2019). Modulation of near-wall turbulence in the transitionally rough regime, *Journal of Fluid Mechanics*, Vol. 865, 1042-1071, doi:10.1017/jfm.2019.41

[14] Güemes, A.; Discetti, S.; Ianiro, A.; Sirmacek, B.; Azizpour, H.; Vinuesa, R. (2021). From coarse wall measurements to turbulent velocity fields through deep learning, *Physics of Fluids*, Vol. 33, No. 7, Paper 075121, 10 pages, doi:10.1063/5.0058346
[15] Cater, J. E.; Williams, J. J. (2008). Large eddy simulation of a long asymmetric compound open channel, *Journal of Hydraulic Research*, Vol. 46, No. 4, 445-453, doi:10.3826/jhr.2008.3134
[16] Zeng, C.; Li, C. W. (2010). A hybrid RANS-LES model for combining flows in open-channel T-junctions, *Journal of Hydrodynamics*, Vol. 22, No. 1, 154-159, doi:10.1016/S1001-6058(09)60186-4
[17] Lam, K.; Lin, Y. F. (2007). Drag force control of flow over wavy cylinders at low Reynolds number, *Journal of Mechanical Science and Technology*, Vol. 21, No. 9, Paper 1331, 7 pages, doi:10.1007/BF03177417
[18] Sudo, K.; Sumida, M.; Hibara, H. (1998). Experimental investigation on turbulent flow in a circular-sectioned 90-degree bend, *Experiments in Fluids*, Vol. 25, No. 1, 42-49, doi:10.1007/s003480050206
[19] Ahmed, F. (2000). Three-dimensional mean velocity analysis of a 30 degree bend flow, *Journal of Engineering Mechanics*, Vol. 126, No. 12, 1262-1272, doi:10.1061/(asce)0733-9399(2000)126:12(1262)
[20] Luo, H.; Fytanidis, D. K.; Schmidt, A. R.; García, M. H. (2018). Comparative 1D and 3D numerical investigation of open-channel junction flows and energy losses, *Advances in Water Resources*, Vol. 117, 120-139, doi:10.1016/j.advwatres.2018.05.012
[21] Xi, B.; Wang, C.; Xi, W.; Liu, Y.; Wang, H.; Yang, Y. (2022). Experimental investigation on the water hammer characteristic of stalling fluid in eccentric casing-tubing annulus, *Energy*, Vol. 253, Paper 124113, 13 pages, doi:10.1016/j.energy.2022.124113
[22] Zeng, C.; Li, C. W. (2010). A hybrid RANS-LES model for combining flows in open-channel T-junctions, *Journal of Hydrodynamics*, Vol. 22, No. 1, 154-159, doi:10.1016/S1001-6058(09)60186-4
[23] Weber, L. J.; Schumate, E. D.; Mawer, N. (2001). Experiments on flow at a 90 open-channel junction, *Journal of Hydraulic Engineering*, Vol. 127, No. 5, 340-350, doi:10.1061/(ASCE)0733-9429(2001)127:5(340)
[24] Du, X.-X.; Lambert, M. F.; Chen, L.; Hu, E. J.; Xi, W. (2020). Pipe burst detection, localization, and quantification using the transient pressure damping method, *Journal of Hydraulic Engineering*, Vol. 146, No. 11, Paper 04020077, 14 pages, doi:10.1061/(asce)hy.1943-7900.0001810
[25] Wang, C.; Chen, X.; Qiu, N.; Zhu, Y.; Shi, W. (2018). Numerical and experimental study on the pressure fluctuation, vibration, and noise of multistage pump with radial diffuser, *Journal of the Brazilian Society of Mechanical Sciences and Engineering*, Vol. 40, No. 10, Paper 481, 15 pages, doi:10.1007/s40430-018-1355-6
[26] Shi, H. X.; Meng, J.; Li, Y. (2021). Numerical simulation of coarse particle two-phase flow in two-stage vortex pump, *International Journal of Simulation Modelling*, Vol. 20, No. 4, 684-695, doi:10.2507/IJSIMM20-4-579
[27] Song, X.; Liu, C. (2021). Experimental study of the floor-attached vortices in pump sump using V3V, *Renewable Energy*, Vol. 164, 752-766, doi:10.1016/j.renene.2020.09.088